Article

Enhancing Free Cyanide Photocatalytic Oxidation by rGO/TiO$_2$ P25 Composites

Elim Albiter [1] [ID]**, Jose M. Barrera-Andrade** [1]**, Lina A. Calzada** [1]**, Jesús García-Valdés** [2,†]**, Miguel A. Valenzuela** [1] [ID] **and Elizabeth Rojas-García** [3,*] [ID]

1 Laboratorio de Catálisis y Materiales, ESIQIE-Instituto Politécnico Nacional, Zacatenco, Ciudad de México 07738, Mexico; ealbitere@ipn.mx (E.A.); jmanban@yahoo.com.mx (J.M.B.-A.); lina_calzada@yahoo.com.mx (L.A.C.); mavalenz@ipn.mx (M.A.V.)
2 Departamento de Química Analítica, Facultad de Química, Universidad Nacional Autónoma de México (UNAM), Ciudad Universitaria, Ciudad de México 04510, Mexico; jesusgv@unam.mx
3 Área de Ingeniería Química, Universidad Autónoma Metropolitana-Iztapalapa, Av. San Rafael Atlixco 186, Col. Vicentina, Iztapalapa, Ciudad de México 09340, Mexico
* Correspondence: erg@xanum.uam.mx
† Diseased.

Abstract: Graphene-TiO$_2$ composites have been investigated in various photocatalytic reactions showing successful synergy compared to pristine TiO$_2$. In the present work, graphene oxide (GO) was synthesized by the Hummers method and then reduced graphene oxide-TiO$_2$ composites (rGO/TiO$_2$) were obtained by an in situ GO photoreduction route. X-ray diffraction, FTIR, Raman, UV–vis DRS, and photoluminescence were the main characterization techniques. The obtained composites containing 1 and 3 wt.% rGO were evaluated in the cyanide (50 mg/L) oxidation and Au-cyanide complex (300 mg/L) degradation under UV-A light. The composites showed higher photocatalytic activity than TiO$_2$, mainly with the 1% rGO content. Cyanate and gold nanoparticles, deposited on the photocatalyst's surface, were the main byproducts during the photocatalyst assessment. The improved photocatalytic activity of the composites was attributed to a higher rate of electron transfer and a lower rate of charge recombination due to the chemical interaction of rGO with TiO$_2$.

Keywords: free cyanide; photocatalytic oxidation; Au–cyanide complex; graphene-TiO$_2$ composites; Raman; FTIR; photoluminescence

1. Introduction

Anionic pollutants, (e.g., nitrate, cyanide, phosphate, fluoride, chromate, arsenate, and vanadate, among others) in water and wastewater have been investigated for decades due to their harmful effect on human health and ecosystems [1]. In particular, cyanides comprise compounds containing the $-C\equiv N$ group, (e.g., HCN, KCN, K$_4$[(Fe(CN)$_6$], CH$_3$CN), which are used in several industries such as mining, food processing, electroplating, coal coking, among others [2]. Free cyanide refers to the cyanide anion (CN$^-$) and the HCN molecule, which coexist in equilibrium in the aqueous phase, depending on pH. For instance, at a pH less than 9.3, most of the total cyanide will exist as HCN molecules, while only the cyanide anion at higher pH will be present (T = 25 °C) [3]. Cyanide ions are commonly found in wastewater in a concentration ranging from 1–500 mg/L, depending on the industry that comes from, which is the most critical that of gold cyanidation solution (>500 mg/L) [4].

Free cyanide toxicity by inhalation, ingestion, or skin contact is well-known in human beings. It works by inhibiting the cytochrome oxidase enzyme, disrupting the process of cellular respiration [3–5]. Concerning the harmful effects of cyanides on living beings, different strategies have been used to eliminate free cyanides by their total conversion into harmless compounds such as carbon dioxide and nitrogen (2CN$^-$ + 2O$_2$ → 2CO$_2$ + N$_2$).

It is common practice to use chemical processes, (e.g., treatment with sulfur dioxide, chlorine, ozone), physical, (e.g., aeration, reverse osmosis), and biological, (e.g., enzymatic degradation), which have advantages and disadvantages in their operation [6–8]. On the other hand, heterogeneous photocatalysis represents a viable green alternative for cyanide degradation in wastewater, which is investigated using a wide variety of catalytic materials under different operating conditions [9,10].

Titanium oxide-based nanomaterials efficiently degrade and mineralize toxic organic and inorganic compounds in wastewater [11]. However, to improve its photocatalytic performance, in terms of the visible light absorption and suppression of charge carriers' recombination, the modification of TiO_2 with carbon materials has shown surprising results [12–16]. Graphene materials possess excellent properties, such as high specific surface area, outstanding charge carrier mobility, high thermal conductivity, high adsorption capacity/electrical conductivity, and high optical transparency. Moreover, they serve as an electron reservoir to accept and transport photogenerated electrons in the semiconductor, enhancing the adsorption capacity for reaction substrates and tuning the composites' light absorption range and intensity [17–19]. As a result, the applications of graphene-based composites in photocatalysis, mainly in the remotion of organic pollutants, have exponentially grown, as observed by the number of publications in the last decade [20,21].

The photocatalytic degradation of free and metal cyanide complexes using graphene/TiO_2 composites is scarce [22]. However, according to previous reports, graphene oxide showed promising applications as a photocatalyst and adsorbent to eliminate free cyanide and other harmful species [23,24]. Therefore, this current study aims to evaluate the photocatalytic oxidation of free cyanide and gold–cyanide by using rGO/TiO_2 composites.

This research aims to increase the photocatalytic activity of TiO_2 by adding reduced graphene oxide (rGO), improving the free cyanide degradation, and removing cyanide and metal simultaneously in a gold–cyanide complex. In this investigation, the effect of adding different amounts of rGO (1 and 3 wt.%) on the interaction with TiO_2 and its role in photocatalytic degradation of free-cyanide and gold–cyanide complex were analyzed. The primary characterization techniques used to support these results were XRD, TEM, Raman, FTIR, photoluminescence, and UV–Vis spectroscopies.

2. Materials and Methods

2.1. Materials

Sulfuric acid (purity > 98%), potassium permanganate, and sodium nitrate (purity > 99.4%) were acquired from J.T.Baker; hydrogen peroxide (30% *v/v*), potassium hydroxide, potassium cyanide (KCN, purity > 97%), and potassium dicyanoaurate (I) (KAu(CN)$_2$) from Sigma-Aldrich, ethylenediaminetetraacetic acid (EDTA) from Alyt brand, isopropyl alcohol, titanium dioxide (P25) from Evonik; tri-distilled mercury from Merck, and industrial-grade graphite. All reagents were used without further purification.

2.2. Preparation of rGO/TiO$_2$ Composites

Firstly, graphene oxide was prepared using the Hummers method [25], and then reduced graphene oxide TiO$_2$ composites (rGO/TiO$_2$) were obtained by an in situ photoreduction method. Briefly, 2 g of TiO$_2$ was added to 100 mL of anhydrous ethanol, and the desired amount of graphene oxide (GO) was included in the suspension to obtain 1 and 3 wt.% GO. The suspension was homogenized in an ultrasound bath (10 min) and then degassed for 5 min in a nitrogen atmosphere. The GO photoreduction was carried out in an UV-light photoreactor (LuzChem, Ottawa, ON, Canada, six low-pressure Hg lamps, $\lambda_{max} = 365$ nm) for 12 h at room temperature (25 °C) under vigorous stirring. Finally, the obtained solids were washed with deionized water and dried at 100 °C for 3 h.

2.3. Characterization

The DR UV–vis spectra were obtained using an Agilent Cary 100 spectrometer (Agilent Technologies, CA, USA) equipped with an integrating sphere. FTIR analyses were

carried out on a NEXUS spectrometer (Thermo Scientific, Waltham, MA, USA) using the transmission KBr pellet technique in the range of 4000 to 400 cm^{-1}. Raman spectra were recorded on an InVia Renishaw system (Renishaw plc., Gloucestershire, UK) equipped with a cooled CCD detector (-73 °C) and a holographic super-Notch filter. The samples were excited with the 532 nm Ar line; the spectral resolution was ca. 4 cm^{-1}, and spectrum acquisition consisted of 5 accumulations of 10 s. The photoluminescence (PL) spectra were obtained in an FLS1000 spectrophotometer (Edinburgh Instruments, Livingston, UK) using an excitation wavelength of 307 nm. The spectra were collected at room temperature with a spectral resolution of 0.5 nm and consisted of 5 accumulations of 0.1 s at each point. The catalyst morphology and particle size analyses were carried out using a scanning electron microscope model JSM6701F (JEOL). Powder samples were analyzed using the secondary electron mode. The textural properties of the catalysts were determined by N$_2$ physisorption measurements at low pressure and 77 K, using an equipment model Autosorb iQ (Quanthachrome, VA, USA). The surface area was calculated using the BET model at $0.05 < P/P_0 < 0.3$ values of the adsorption isotherms. Moreover, the BJH model was used to estimate the pore size and volume from the desorption isotherms data.

2.4. Photocatalytic Evaluation

The photocatalytic degradation of free cyanide (CN$^-$) and the gold–cyanide complex was carried out in a 100 mL glass cell under UV light irradiation (LuzChem photoreactor, six lamps, λ_{max} = 365 nm). In a typical experiment, 50 mg of catalyst were suspended, using an ultrasonic bath, in 50 mL of a KCN solution (50 ppm, pH = 12). After, a 400 mL/min airflow was injected into the glass cell space in total darkness under constant magnetic stirring for 30 min (adsorption–desorption process), and then the UV lamps were turned on. During the experiment, aliquots were taken every 30 min and filtered using a 0.2 μm filter (Millipore) to remove the catalyst. CN$^-$ and cyanate ions were quantified in each sample using the differential pulse polarography (DPP) technique (797 VA computrace, Metrohm).

In the case of the gold–cyanide complex degradation experiments, an aqueous solution of KAu(CN)$_2$ (300 ppm) and 500 μL of isopropyl alcohol as a sacrificial agent, and the experimentation followed the same protocol used for the degradation of free cyanides. The DPP technique was also used to analyze the [Au(CN)$_2$]$^-$ ion concentration, and it is the first time this technique has been reported in monitoring the Au–CN complex. Detailed information on the DPP technique analysis of free cyanide and cyanate is in the Supplementary Information (SI).

3. Results and Discussion

3.1. Characterization

The coexistence of rGO and TiO$_2$ in the composite materials was detected by Raman spectroscopy. Figure 1a shows the Raman spectra of the TiO$_2$, GO, and composite materials. In the TiO$_2$ Raman spectrum, several bands are observed around 144, 396, 517, and 638 cm^{-1} characteristics of the E$_g$, B$_{1g}$, A$_{1g}$ + B$_{1g}$, and E$_g$ vibrational modes of anatase phase, respectively [26]. At the same time, two bands at 445 and 605 cm^{-1} were detected and attributed to the rutile phase's E$_g$ and A$_{1g}$ modes. Graphene oxide (GO) has two characteristic signals at 1350 and 1600 cm^{-1} corresponding to the D and G bands. The D band is associated with sp^3 defects within the hexagonal graphitic structure. In contrast, the G band is characteristic of sp^2 hybridized carbon materials, providing information on the plane vibration of sp^2 bonded carbon domains [27]. The D and G band ratio (I$_D$/I$_G$) is a parameter that indicates the disorder degree in the graphitic structure or edge. The I$_D$/I$_G$ ratio calculated for the materials were 1.56, 0.99, 1.04, and 1.36 for GO, rGO, 1.0 rGO/TiO$_2$ and 3.0 rGO/TiO$_2$. As can be seen, the 1.0 rGO/TiO$_2$ composite shows the lowest I$_D$/I$_G$ ratio, smaller than that of GO, indicating an interaction between GO and TiO$_2$ through π–π stacking. This decrease reveals an increase in sp^2 domains in the carbon atoms planes due to decreasing unsaturated defects atoms in the GO by eliminating oxygenated functional groups and thus transforming GO to rGO [28–30].
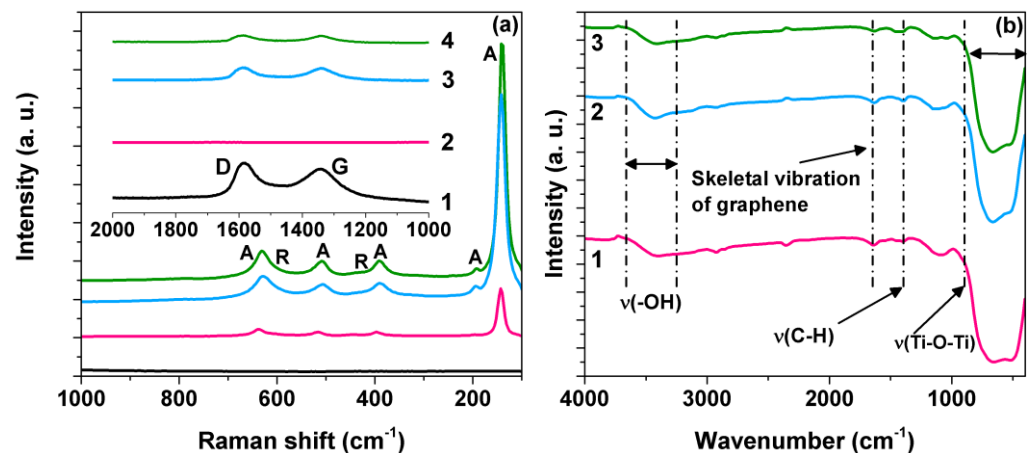
Figure 1. (**a**) Raman spectra of (1) graphene oxide, (2) TiO_2 P25 (3) 1.0rGO/ TiO_2, and (4) 3.0rGO/TiO_2. (**b**) FTIR spectra of (1) TiO_2 P25, (2) 1.0rGO/TiO_2, and (3) 3.0rGO/TiO_2. A: anatase, R: rutile.

FT-IR spectra of the TiO_2 and rGO/TiO_2 composite materials are displayed in Figure 1b and the GO spectrum are illustrated in Figure S1 (SI). In the GO spectrum, a broadband center at 3410 cm^{-1} is observed, characteristic of stretching vibrations of the $^-$OH bond due to adsorbed water molecules on the surface. Furthermore, the GO absorption spectrum also presented bands around 1721, 1574, 1389, and 1047 cm^{-1}, attributable to stretching vibrations of carbonyl/carboxyl groups (C=O) present in the edges of graphitic layers, skeletal vibration of the graphene, bending vibration of tertiary C-OH hydroxyl groups, and stretching vibrations of =C-H groups, respectively [30,31]. Figure 1b shows FTIR spectra of TiO_2 and composite materials in which a broad absorption band appears around 3409 cm^{-1}, characteristic of the O-H stretching vibration of $^-$OH groups or adsorbed water. Other bands are perceived around 1579 and 1383 cm^{-1}, which are characteristic of skeletal vibration of the graphene and C-H vibration, respectively. Additionally, a broad absorption band between 400 and 1000 cm^{-1} is detected in the FTIR spectra of TiO_2 and rGO/TiO_2 corresponding to Ti-O-Ti vibrations.

However, it has been a point of debate in recent years to determine the band's position corresponding to the interaction of TiO_2 nanoparticles and rGO sheets via the possible formation of the Ti-O-C bond [32,33]. Thus, this zone was deconvoluted, and the results are displayed in Figure 2a–d. It can be noted that the broad absorption band between 400 and 1000 cm^{-1} for TiO_2 and the composite materials show three components at 489, 660, and 783 cm^{-1}, which have been assigned to Ti-O-Ti vibrations [34,35]. Furthermore, a displacement in the band position at 489 cm^{-1} to higher wavenumbers for 1.0rGO/TiO_2 and 3.0rGO/TiO_2 composites were observed, possibly due to a chemical interaction between TiO_2 nanoparticles and rGO [30,36]. Interestingly, our FTIR results do not support the formation of a Ti-O-C bond since the deconvolution analysis in the 1000 cm^{-1} region always showed three components, even though the rGO is not present in the photocatalyst.

The presence of Ti-O-C bonds improves the separation of photogenerated electrons and holes after light irradiation, decreasing the charge carrier's recombination and giving rise to a higher photocatalytic activity [31,34]. The deconvolution of the Raman spectra was performed in the range of 300 and 800 cm^{-1} for TiO_2 and composite materials to support a Ti-O-C bond formation, as shown in Figure 2d–f. As can be seen, three components at 635 (E_g), 516 ($A_{1g} + B_{1g}$), and 396 (B_{1g}) cm^{-1} correspond to the anatase phase, and two components at 608 (A_{1g}) and 433 (E_g) cm^{-1} belong to the rutile phase, in the deconvolution of the Raman spectra are observed. The intensity of these last two components decreases with the increment of the rGO content. Additionally, an increase in the full width at half maximum (FWHM) of the rutile A_{1g} and E_g Raman peaks in the composite materials was observed (Figure 2e). Shahbazi et al. [37] attributed the widening of the rutile E_g

Raman peak to the distortion of the titania framework host due to the introduction of rGO into the titania lattice.
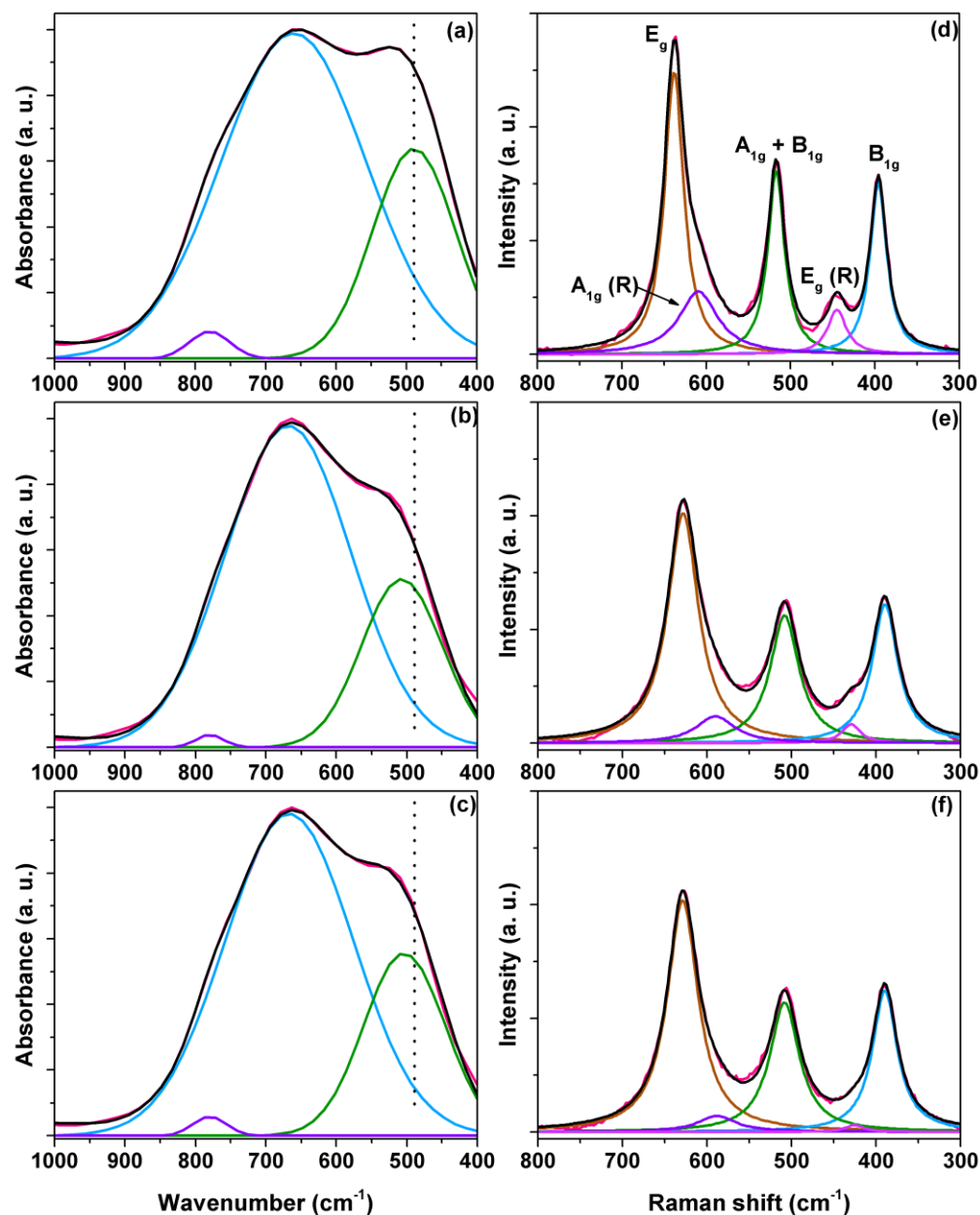

Figure 2. (**a**–**c**) Deconvolution of FTIR spectra of TiO_2, 1.0rGO/TiO_2, and 3.0rGO/TiO_2, respectively. (**d**–**f**) Deconvolution of Raman spectra of TiO_2 Evonik, 1.0rGO/TiO_2, and 3.0rGO/TiO_2, respectively. A: anatase, R: rutile.

The photocatalysts were characterized using UV–Vis diffuse reflectance spectroscopy to know the effect of the amount of rGO in the composite materials on the optical properties. The composite materials' optical bandgap was determined using the Tauc model [38], Figure 3a–c. The bandgap was obtained by plotting a tangent line to the point of inflection of the curve of the graph $(\alpha h v)^{1/2}$ vs. $h v$ (energy), where $(\alpha h v)^{1/2} = 0$. A decrease (redshift) was observed, due to the incorporation of the rGO into the TiO_2 P25 (3.08 eV). The resulting bandgap values for the composite materials were: 2.18 and 2.19 eV for 1% rGO, and 3% rGO, respectively. Other studies have reported the same behavior [30,34]. This decrease in the bandgap could be attributed to the chemical interaction between the TiO_2 nanoparticles and

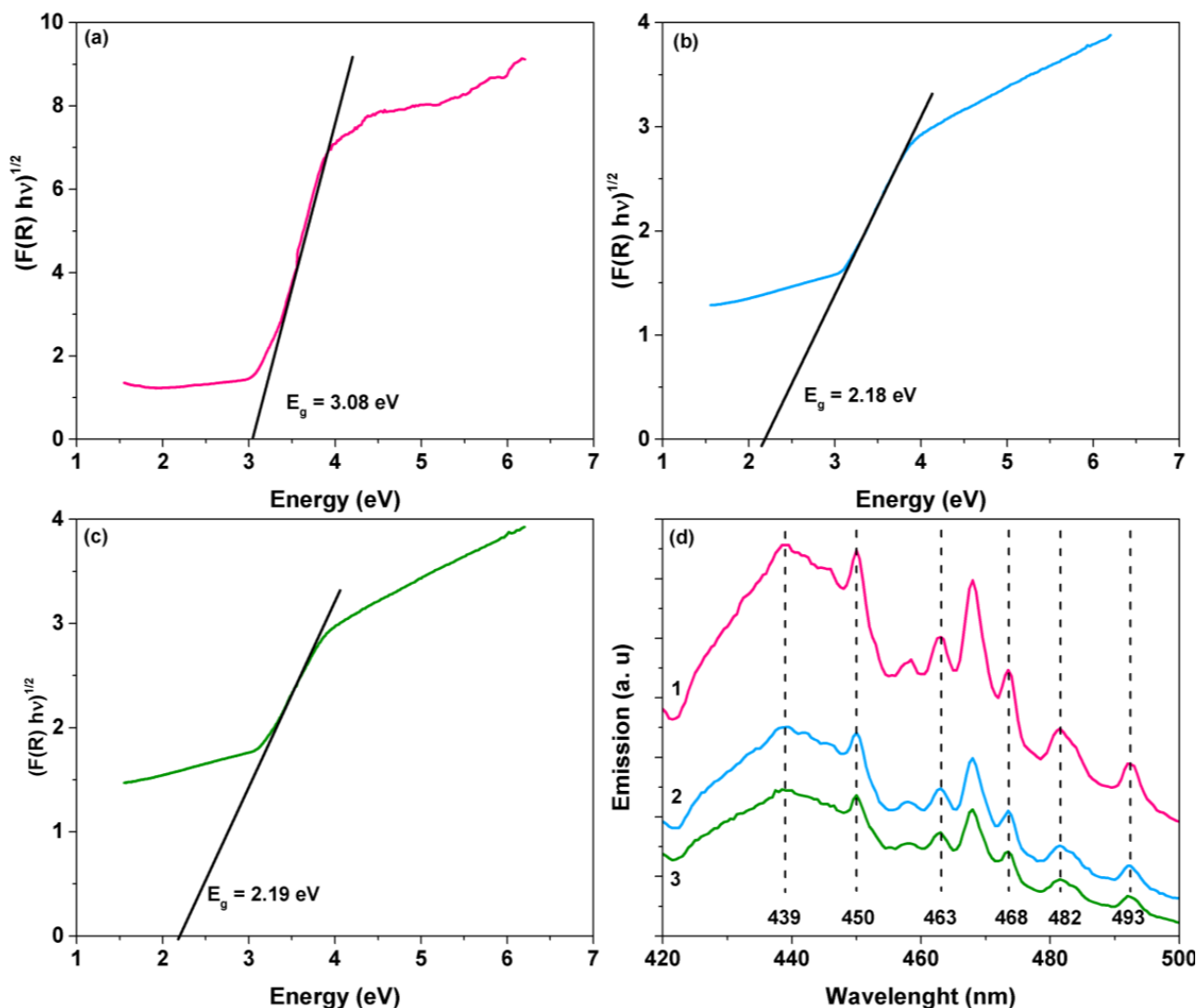rGO nanolayers, resulting in increased photocatalytic activity in the composites compared to pristine TiO_2.

Figure 3. Tauc plots for the determination of optical band gap of (**a**) TiO_2, (**b**) 1.0rGO/TiO_2, and (**c**) 3.0rGO/TiO_2, respectively. (**d**) PL spectra of (1) TiO_2 P25, (2) 1.0rGO/TiO_2, and (3) 3.0rGO/TiO_2.

The photoluminescence spectra of TiO_2 and rGO/TiO_2 composites were determined at steady-state and room temperature under an excitation wavelength of 307 nm (Figure 3d) to verify the charge carriers' recombination process. The presence of rGO in the composites causes a decrease in the PL intensity, depending on its loading. This behavior could be explained by suppressing the electron–hole recombination in the TiO_2 [39]. Additionally, the peaks at PL spectra can be ascribed to several defects due to self-trapped excitons, oxygen vacancies, or other surface states [40]. For example, the peaks at 439 nm could be assigned to the self-trapped exciton caused by the de-excitation of Ti^{3+}_{3d} electrons to the valence band [41]. The same can be said for the 450, 463, and 468 nm signals. Finally, the peaks at 482 and 493 nm could be caused by oxygen vacancies [41].

TiO_2 (Figure S3a) indicates the presence of a nanometric powder made of dense and equiaxial particles exhibiting a particle diameter of ca. 30 nm. The analyses by scanning electron microscopy and nitrogen physisorption were performed to know the effect that the addition of rGO to TiO_2 has on the bulk and surface properties, respectively. Figure S3 shows the SEM analysis of the samples. The morphology and observed primary particle size

did not change significantly in the samples of 1.0rGO/TiO$_2$ (Figure S3b) and 3.0rGO/TiO$_2$ (Figure S3c). However, certain agglomerates were observed, attributed to the incorporation of the rGO phase, which the TiO$_2$ must cover as the former is present in the sample as a minority component. Generally, the obtained samples are homogeneous, with no phase segregation observed.

Figure S4 shows the obtained N$_2$ adsorption/desorption isotherms. Based on the UIPAC classification, TiO$_2$ exhibits a type II isotherm characteristic of dense, non-porous solids. This result agrees with SEM observations. Moreover, the specific surface area values were calculated using the BET model and are presented in Table S1. As expected, incorporating rGO into the TiO$_2$ promotes a higher specific surface area for the 3.0rGO sample. Some changes are observed in the isotherms profile, wherein the hysteresis loop area increases as the rGO increases; in the same sense, an increase in the pore volume is evidenced due to the incorporation of the rGO on TiO$_2$ particles.

3.2. Photocatalytic Activity

Before the photocatalytic evaluation, three blank experiments were performed. First, no cyanide losses were observed by volatilization in the reaction medium at pH = 12 after three hours. Second, the cyanide conversion in the absence of a photocatalyst was negligible, even under UV light irradiation. Third, the cyanide reaction in the presence of the photocatalyst, but without UV light, did not proceed. Additionally, CN$^-$ adsorption was performed on TiO$_2$ and rGO/TiO$_2$ composites; in these experiments, the CN$^-$ concentration decreased ca. 10% after 60 min in the dark, under constant stirring. The only byproduct detected in the whole irradiation time was the cyanate ion.

The degradation profiles of CN$^-$ and cyanate ions (CNO$^-$) using TiO$_2$ and the rGO/TiO$_2$ catalysts are presented in Figure 4. Interestingly, complete cyanide degradation was observed with all photocatalysts at different irradiation times, depending on the rGO concentration in the composites. For example, TiO$_2$ required 335 min of irradiation to achieve the total cyanide conversion. Similar results were obtained by Kim et al. [42] but using 30 ppm of cyanide and irradiating with a UV-C lamp (180–280 nm). Note that the concentration profiles, (i.e., cyanide and cyanate) by using TiO$_2$ (Figure 5a) or the rGO/TiO$_2$ photocatalysts (Figure 5b,c) seem the same. Still, a faster reaction rate can be observed and corroborated by the shorter degradation time required (150–180 min). As a result, the presence of rGO improves the photocatalytic activity of TiO$_2$ significantly, transforming CN$^-$ into CNO$^-$, a less toxic byproduct (CN$^-$ + 2OH → CNO$^-$ + H$_2$O).

A photocatalyst's stability and reusability are essential in determining catalytic materials' practical utility. Thus, high stability is shown by the 1% rGO/TiO$_2$ composite after five cycling tests are worth noting, which lost three percentage points after the third cycle and subsequently remained constant, indicating the composite's robustness in the highly alkaline medium (Figure 4d).

Under our experimental conditions, cyanide degradation followed pseudo-first-order kinetics independently of the used photocatalyst. The calculated values, in min^{-1}, of the apparent reaction rate constant (k) were 0.0052, 0.0115, and 0.0107 for TiO$_2$, 1.0rGO/TiO$_2$, and 3.0rGO/TiO$_2$, respectively. According to these values, the best photocatalyst was 1.0 rGO/TiO$_2$. This behavior has been previously observed in other rGO/TiO$_2$ composites, where an excess of rGO decreased the photocatalytic performance of the materials [43,44]. This decrease is normally attributed to the higher rGO coverage of the TiO$_2$ surface, which reduces the semiconductor's light absorption.

Two routes are known to achieve the photocatalytic oxidation of cyanides in an aqueous solution at high pH (>10): indirect, which employs the photogenerated OH radicals in a homogeneous phase, and direct, by using the trapped holes at the surface hydroxyls groups [45]. Even though we have no evidence to support one or the other conversion pathway for cyanides, the presence of rGO improved the TiO$_2$ photoactivity, which could be linked to a higher ROS (O$_2$·, HO$_2$·, HO·, among others) formation due to a reduced electron–hole pairs recombination rate [28]
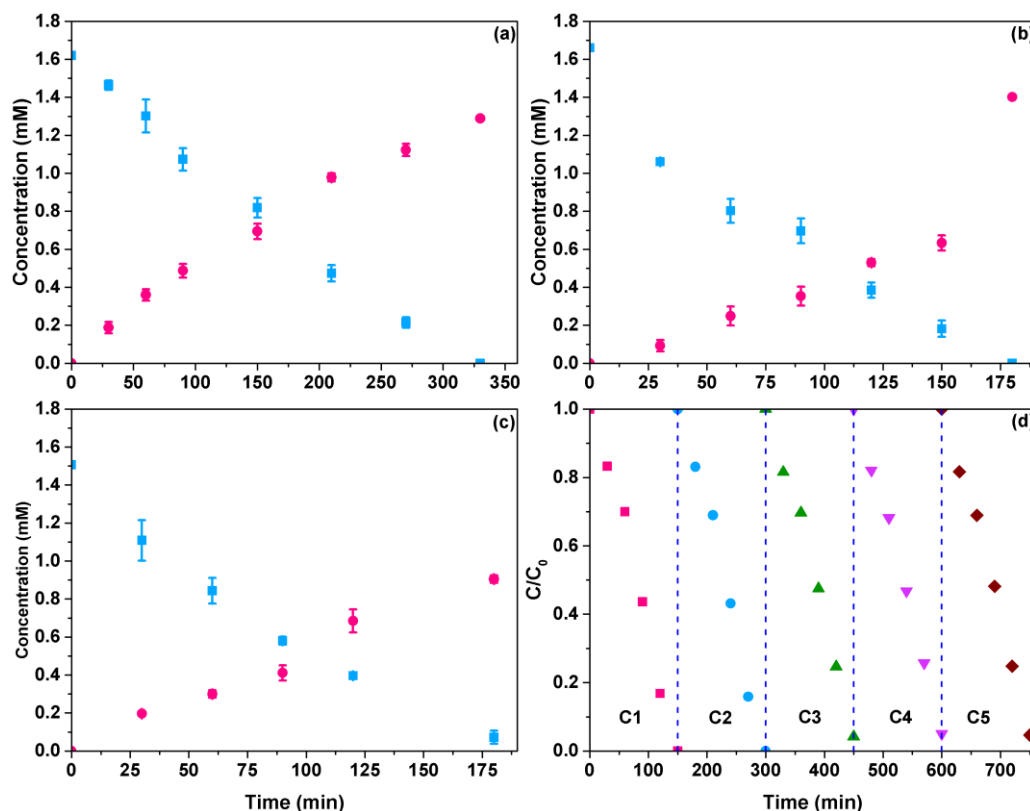
Figure 4. Degradation profiles of cyanide (■) and formation profiles of cyanate (●) using TiO_2 and rGO/TiO_2 composites: (**a**) TiO_2, (**b**) 1.0rGO/TiO_2, (**c**) 3.0rGO/TiO_2. (**d**) The efficiency of cyanide photocatalytic oxidation in five cycles of the 1.0rGO/TiO_2 composite.
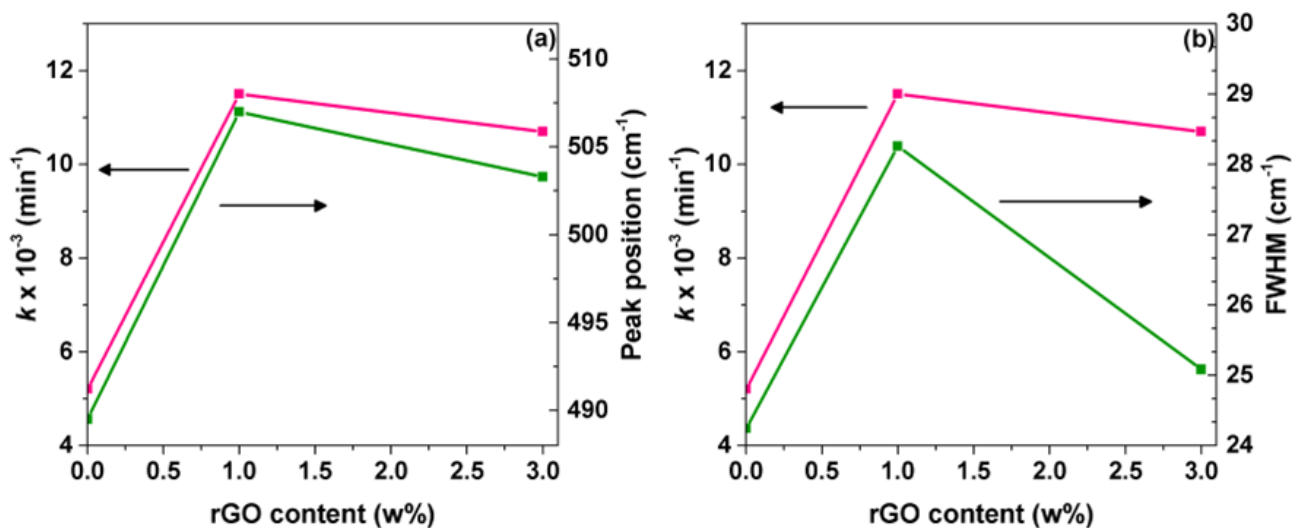

Figure 5. Influence of the composite's rGO content on the reaction constant, (**a**) influence of the rGO content on the Ti-O-Ti stretching vibration peak position in the FTIR, (**b**) influence of the rGO content on the FWHM of the Rutile Eg Raman peak.

As mentioned before, adding small amounts of rGO to TiO_2 modifies its optical properties, confirming the chemical interaction between the two species. In other words, the observed slight changes in the TiO_2 peak position (FTIR) and an increase in the FWHM of the Rutile Raman peak in the composite materials can be correlated with the rate constant for CN^- photocatalytic oxidation, as is shown in Figure 5.

This work introduces the results of the photocatalytic degradation of the Au–CN complex using rGO/TiO$_2$ composites. The degradation profiles of the Au–CN complex (potassium dicyanoaurate at an initial concentration of 300 ppm) are shown in Figure 6a. The metal complex was degraded in the presence of isopropyl alcohol (10 mM) as a sacrificial electron donor and ambient air. Under these experimental conditions, the reduction in the gold–cyanide complex forms metallic gold and free cyanide according to the following reaction [46]: $Au(CN)_2^- + e^- \rightarrow Au + 2\,CN^-$.
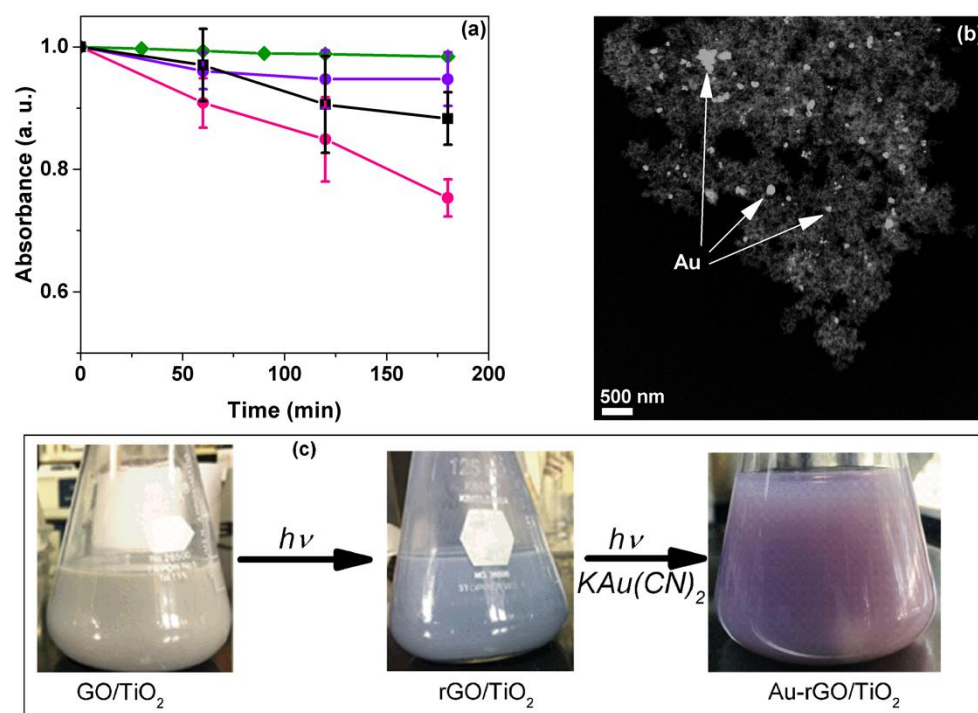

Figure 6. (**a**) Degradation profiles of Au(CN)$_2^-$ complex using rGO/TiO$_2$ composites: (♦) photolysis, (•) TiO$_2$ P25, (•) 1.0rGO/TiO$_2$, and (■)3.0rGO/TiO$_2$. (**b**) Dark field TEM image of the rGO/TiO$_2$ composites after Au–N complex degradation. (**c**) Color changes during the synthesis of the rGO/TiO$_2$ composite and degradation of the Au–CN complex.

Experimental evidence of the gold-cyanide degradation is presented in Figure 6b. A dark field TEM micrograph shows that gold particles appear deposited on the 1% rGO/TiO$_2$ catalyst with different sizes. Note that the Au–CN complex degraded linearly with a clear dependence on the rGO amount. Surprisingly, the higher photocatalytic degradation (~30%) was obtained with the 1% rGO/TiO$_2$, and the TiO$_2$ presents a negligible conversion of the Au–CN complex. An increment in the rGO content in the composite materials (3% rGO/TiO$_2$) and a decrease in photocatalytic activity were observed. This decrease could be due to the strong absorption of light or competition for light capture between reduced graphene oxide and TiO$_2$. Figure 6c shows the various stages of the evolution of the graphene/TiO$_2$ composites, from the integration of GO (sand color) to its transformation into rGO by photocatalytic reduction (gray color), and the deposit of gold particles on the composite (purple color). These results demonstrate an improvement of the photocatalytic activity of TiO$_2$ again by adding rGO, which could explain a decrease in the recombination rate of electron–hole pairs, allowing the decomposition of a highly stable Au–CN complex.

A schematic proposal to explain the Au–CN complex photocatalytic reduction is presented in Figure 7. The first step consists of the Au(CN)$_2^-$ anion adsorption on the composite's surface in an aqueous solution at pH 12 [47,48]. In the second step, UV light irradiation starts with the generation of the electron–hole pairs and promotes the Au(CN)$_2^-$ reduction and isopropyl alcohol oxidation, respectively. Experimental evidence of these reactions was the metallic gold particles deposited on the composite and the initial

generation of acetone from isopropyl alcohol oxidation. In the third step, the deposited Au particles enhanced the photocatalytic oxidation of formed cyanide ions (Equation (3)) to cyanate. The fourth stage corresponds to the reaction between surface hydroxyls linked to TiO_2 and the photogenerated holes producing OH radicals (Equation (4)). The subsequent steps (Equations (5)–(7)) involve reactions of the other radicals formed with the cyanide for its transformation into cyanate.
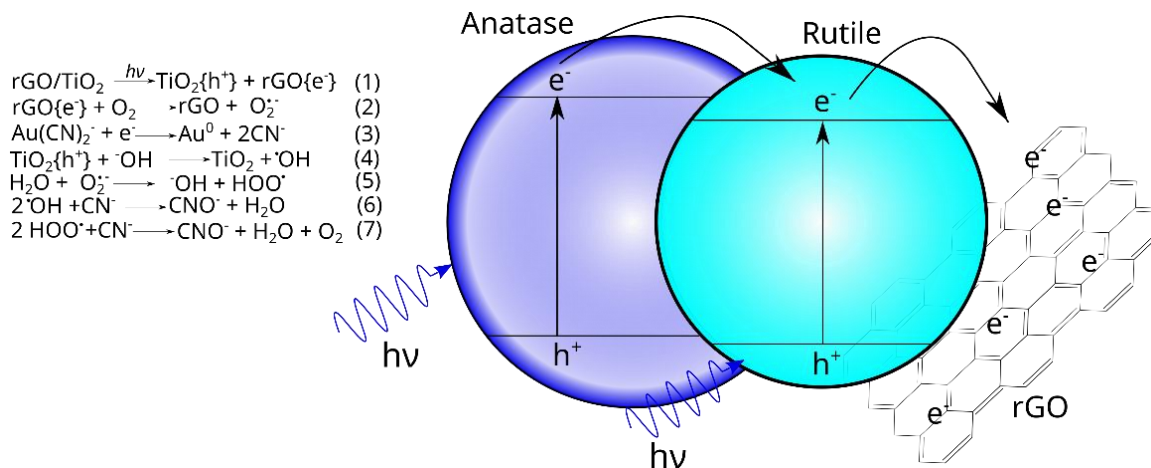
$$rGO/TiO_2 \xrightarrow{h\nu} TiO_2\{h^+\} + rGO\{e^-\} \quad (1)$$
$$rGO\{e^-\} + O_2 \longrightarrow rGO + O_2^{\cdot-} \quad (2)$$
$$Au(CN)_2^- + e^- \longrightarrow Au^0 + 2CN^- \quad (3)$$
$$TiO_2\{h^+\} + {}^-OH \longrightarrow TiO_2 + {}^{\cdot}OH \quad (4)$$
$$H_2O + O_2^{\cdot-} \longrightarrow {}^-OH + HOO^{\cdot} \quad (5)$$
$$2{}^{\cdot}OH + CN^- \longrightarrow CNO^- + H_2O \quad (6)$$
$$2\,HOO^{\cdot} + CN^- \longrightarrow CNO^- + H_2O + O_2 \quad (7)$$

Figure 7. A schematic diagram showing the various steps for the Au–CN complex degradation in the presence of the rGO-TiO_2 P25 composite under UV light.

4. Conclusions

The photocatalytic reduction of graphene oxide successfully obtained reduced graphene oxide/TiO_2 composites. Both composites presented a higher photocatalytic activity on free cyanide oxidation than TiO_2, but 1% rGO loaded to TiO_2 showed the best performance. The enhanced activity was attributed to the interaction between the rGO and TiO_2, as evidenced by Raman, FTIR and UV–Vis, and photoluminescence studies. This interaction would reduce the charge carrier's recombination rate, leading to an effective activation of TiO_2 by UV irradiation and an enhanced charge transfer between RGO and TiO_2, increasing the photocatalytic activity measured as cyanide degradation. In addition, the optical properties of the composites revealed a chemical interaction (Ti-O-C) between the TiO_2 and rGO, which was correlated with the rate constant in the photocatalytic oxidation of cyanide.

Additionally, the rGO/TiO_2 composites showed higher activity than TiO_2 in the degradation of the Au–CN complex at high initial concentrations (300 ppm). The Au$^-$ ion was successfully reduced and deposited on the surface of TiO_2, as evidenced by TEM analysis.

Author Contributions: Conceptualization, M.A.V.; methodology, J.M.B.-A. and J.G.-V.; investigation, J.M.B.-A., E.A., E.R.-G., L.A.C. and M.A.V.; writing—original draft preparation, J.M.B.-A. and E.R.-G.; writing—review and editing, E.A., L.A.C. and M.A.V.; funding acquisition, E.A. and M.A.V. All authors have read and agreed to the published version of the manuscript.

Conflicts of Interest: The authors declare no conflict of interest.

References

1. Xu, X.; Gao, B.; Jin, B.; Yue, Q. Removal of Anionic Pollutants from Liquids by Biomass Materials: A Review. *J. Mol. Liq.* **2016**, *215*, 565–595. [CrossRef]
2. Dash, R.R.; Gaur, A.; Balomajumder, C. Cyanide in Industrial Wastewaters and Its Removal: A Review on Biotreatment. *J. Hazard. Mater.* **2009**, *163*, 1–11. [CrossRef] [PubMed]
3. Johnson, C.A. The Fate of Cyanide in Leach Wastes at Gold Mines: An Environmental Perspective. *Appl. Geochem.* **2015**, *57*, 194–205. [CrossRef]
4. Jaszczak, E.; Polkowska, Ż.; Narkowicz, S.; Namieśnik, J. Cyanides in the Environment—Analysis—Problems and Challenges. *Environ. Sci. Pollut. Res.* **2017**, *24*, 15929–15948. [CrossRef] [PubMed]
5. Kjeldsen, P. Behaviour of Cyanides in Soil and Groundwater: A Review. *Water. Air. Soil Pollut.* **1999**, *115*, 279–308. [CrossRef]
6. Sharma, M.; Akhter, Y.; Chatterjee, S. A Review on Remediation of Cyanide Containing Industrial Wastes Using Biological Systems with Special Reference to Enzymatic Degradation. *World J. Microbiol. Biotechnol.* **2019**, *35*, 70. [CrossRef] [PubMed]
7. Baral, A.; Das, D.P.; Minakshi, M.; Ghosh, M.K.; Padhi, D.K. Probing Environmental Remediation of RhB Organic Dye Using α-MnO$_2$ under Visible- Light Irradiation: Structural, Photocatalytic and Mineralization Studies. *ChemistrySelect* **2016**, *1*, 4277–4285. [CrossRef]
8. Baral, A.B.; Dash, B.; Ghosh, M.K.; Subbaiah, T.; Minakshi, M. Pathway of Sucrose Oxidation in Manganese (Pyrolusite) Nodule. *Ind. Eng. Chem. Res.* **2015**, *54*, 12233–12241. [CrossRef]
9. Betancourt-Buitrago, L.A.; Hernandez-Ramirez, A.; Colina-Marquez, J.A.; Bustillo-Lecompte, C.F.; Rehmann, L.; Machuca-Martinez, F. Recent Developments in the Photocatalytic Treatment of Cyanide Wastewater: An Approach to Remediation and Recovery of Metals. *Processes* **2019**, *7*, 225. [CrossRef]
10. Bouras, D.; Mecif, A.; Barillé, R.; Harabi, A.; Rasheed, M.; Mahdjoub, A.; Zaabat, M. Cu:ZnO Deposited on Porous Ceramic Substrates by a Simple Thermal Method for Photocatalytic Application. *Ceram. Int.* **2018**, *44*, 21546–21555. [CrossRef]
11. Chen, D.; Cheng, Y.; Zhou, N.; Chen, P.; Wang, Y.; Li, K.; Huo, S.; Cheng, P.; Peng, P.; Zhang, R.; et al. Photocatalytic Degradation of Organic Pollutants Using TiO$_2$-Based Photocatalysts: A Review. *J. Clean. Prod.* **2020**, *268*, 121725. [CrossRef]
12. Leary, R.; Westwood, A. Carbonaceous Nanomaterials for the Enhancement of TiO$_2$ Photocatalysis. *Carbon* **2011**, *49*, 741–772. [CrossRef]
13. Kusiak-Nejman, E.; Morawski, A.W. TiO$_2$/Graphene-Based Nanocomposites for Water Treatment: A Brief Overview of Charge Carrier Transfer, Antimicrobial and Photocatalytic Performance. *Appl. Catal. B Environ.* **2019**, *253*, 179–186. [CrossRef]
14. Morales-Torres, S.; Pastrana-Martínez, L.M.; Figueiredo, J.L.; Faria, J.L.; Silva, A.M.T. Design of Graphene-Based TiO$_2$ Photocatalysts—a Review. *Environ. Sci. Pollut. Res.* **2012**, *19*, 3676–3687. [CrossRef] [PubMed]
15. Mohamed, H.H.; Alsanea, A.A. TiO$_2$/Carbon Dots Decorated Reduced Graphene Oxide Composites from Waste Car Bumper and TiO$_2$ Nanoparticles for Photocatalytic Applications. *Arab. J. Chem.* **2020**, *13*, 3082–3091. [CrossRef]
16. Manickam, M.; Singh, P.; Issa, T.B.; Thurgate, S. Electrochemical Behavior of Anatase TiO$_2$ in Aqueous Lithium Hydroxide Electrolyte. *J. Appl. Electrochem.* **2006**, *36*, 599–602. [CrossRef]
17. Zhang, N.; Xu, Y.-J. The Endeavour to Advance Graphene–Semiconductor Composite-Based Photocatalysis. *CrystEngComm* **2015**, *18*, 24–37. [CrossRef]
18. Mamba, G.; Gangashe, G.; Moss, L.; Hariganesh, S.; Thakur, S.; Vadivel, S.; Mishra, A.K.; Vilakati, G.D.; Muthuraj, V.; Nkambule, T.T.I. State of the Art on the Photocatalytic Applications of Graphene Based Nanostructures: From Elimination of Hazardous Pollutants to Disinfection and Fuel Generation. *J. Environ. Chem. Eng.* **2020**, *8*, 103505. [CrossRef]
19. Rasheed, M.; Shihab, S.; Sabah, O.W. An Investigation of the Structural, Electrical and Optical Properties of Graphene-Oxide Thin Films Using Different Solvents. *J. Phys. Conf. Ser.* **2021**, *1795*, 012052. [CrossRef]
20. Singh, P.; Shandilya, P.; Raizada, P.; Sudhaik, A.; Rahmani-Sani, A.; Hosseini-Bandegharaei, A. Review on Various Strategies for Enhancing Photocatalytic Activity of Graphene Based Nanocomposites for Water Purification. *Arab. J. Chem.* **2020**, *13*, 3498–3520. [CrossRef]
21. Thakur, K.; Kandasubramanian, B. Graphene and Graphene Oxide-Based Composites for Removal of Organic Pollutants: A Review. *J. Chem. Eng. Data* **2019**, *64*, 833–867. [CrossRef]
22. Zhang, Y.; Zhang, Y.; Huang, Y.; Chen, X.; Cui, H.; Wang, M. Enhanced Photocatalytic Reaction and Mechanism for Treating Cyanide-Containing Wastewater by Silicon-Based Nano-Titania. *Hydrometallurgy* **2020**, *198*, 105512. [CrossRef]
23. Barrera-Andrade, J.M.; Rojas-García, E.; García-Valdés, J.; Valenzuela, M.A.; Albiter, E. Incorporation of Amide Functional Groups to Graphene Oxide during the Photocatalytic Degradation of Free Cyanide. *Mater. Lett.* **2020**, *280*, 128538. [CrossRef]
24. Yang, L.; Jia, F.; Yang, B.; Song, S. Efficient Adsorption of Au(CN)$_2^-$ from Gold Cyanidation with Graphene Oxide-Polyethylenimine Hydrogel as Adsorbent. *Results Phys.* **2017**, *7*, 4089–4095. [CrossRef]
25. Hummers, W.S.; Offeman, R.E. Preparation of Graphitic Oxide. *J. Am. Chem. Soc.* **1958**, *80*, 1339. [CrossRef]

26. Liang, D.; Cui, C.; Hu, H.; Wang, Y.; Xu, S.; Ying, B.; Li, P.; Lu, B.; Shen, H. One-Step Hydrothermal Synthesis of Anatase TiO_2/Reduced Graphene Oxide Nanocomposites with Enhanced Photocatalytic Activity. *J. Alloys Compd.* **2014**, *582*, 236–240. [CrossRef]

27. Kudin, K.N.; Ozbas, B.; Schniepp, H.C.; Prud'homme, R.K.; Aksay, I.A.; Car, R. Raman Spectra of Graphite Oxide and Functionalized Graphene Sheets. *Nano Lett.* **2008**, *8*, 36–41. [CrossRef] [PubMed]

28. Tolosana-Moranchel, A.; Casas, J.A.; Bahamonde, A.; Pascual, L.; Granone, L.I.; Schneider, J.; Dillert, R.; Bahnemann, D.W. Nature and Photoreactivity of TiO_2-RGO Nanocomposites in Aqueous Suspensions under UV-A Irradiation. *Appl. Catal. B Environ.* **2019**, *241*, 375–384. [CrossRef]

29. Shen, J.; Yan, B.; Shi, M.; Ma, H.; Li, N.; Ye, M. One Step Hydrothermal Synthesis of TiO_2-Reduced Graphene Oxide Sheets. *J. Mater. Chem.* **2011**, *21*, 3415–3421. [CrossRef]

30. Chen, Y.; Gao, H.; Xiang, J.; Dong, X.; Cao, Y. Enhanced Photocatalytic Activities of TiO_2-Reduced Graphene Oxide Nanocomposites Controlled by TiOC Interfacial Chemical Bond. *Mater. Res. Bull.* **2018**, *99*, 29–36. [CrossRef]

31. Khamboonrueang, D.; Srirattanapibul, S.; Tang, I.-M.; Thongmee, S. TiO_2·rGO Nanocomposite as a Photo Catalyst for the Reduction of Cr^{6+}. *Mater. Res. Bull.* **2018**, *107*, 236–241. [CrossRef]

32. Gillespie, P.N.O.; Martsinovich, N. Origin of Charge Trapping in TiO_2/Reduced Graphene Oxide Photocatalytic Composites: Insights from Theory. *ACS Appl. Mater. Interfaces* **2019**, *11*, 31909–31922. [CrossRef] [PubMed]

33. Zhang, Y.; Pan, C. TiO_2/Graphene Composite from Thermal Reaction of Graphene Oxide and Its Photocatalytic Activity in Visible Light. *J. Mater. Sci.* **2011**, *46*, 2622–2626. [CrossRef]

34. Zhang, Y.; Hou, X.; Sun, T.; Zhao, X. Calcination of Reduced Graphene Oxide Decorated TiO_2 Composites for Recovery and Reuse in Photocatalytic Applications. *Ceram. Int.* **2017**, *43*, 1150–1159. [CrossRef]

35. Ruidíaz-Martínez, M.; Álvarez, M.A.; López-Ramón, M.V.; Cruz-Quesada, G.; Rivera-Utrilla, J.; Sánchez-Polo, M. Hydrothermal Synthesis of RGO-TiO_2 Composites as High-Performance UV Photocatalysts for Ethylparaben Degradation. *Catalysts* **2020**, *10*, 520. [CrossRef]

36. Li, W.; Liu, X.; Li, H. Hydrothermal Synthesis of Graphene/Fe^{3+}-Doped TiO_2 Nanowire Composites with Highly Enhanced Photocatalytic Activity under Visible Light Irradiation. *J. Mater. Chem. A* **2015**, *3*, 15214–15224. [CrossRef]

37. Shahbazi, R.; Payan, A.; Fattahi, M. Preparation, Evaluations and Operating Conditions Optimization of Nano TiO_2 over Graphene Based Materials as the Photocatalyst for Degradation of Phenol. *J. Photochem. Photobiol. Chem.* **2018**, *364*, 564–576. [CrossRef]

38. Tauc, J.; Menth, A. States in the Gap. *J. Non-Cryst. Solids* **1972**, *8–10*, 569–585. [CrossRef]

39. Sui, X.; Li, X.; Ni, T.; Lin, F.; Li, G. Carbonaceous–TiO_2 Materials: Unique Morphologies for Photocatalytic Applications. *J. Mater. Sci.* **2020**, *55*, 2725–2740. [CrossRef]

40. Liu, B.; Zhao, X.; Wen, L. The Structural and Photoluminescence Studies Related to the Surface of the TiO_2 Sol Prepared by Wet Chemical Method. *Mater. Sci. Eng. B* **2006**, *134*, 27–31. [CrossRef]

41. Biswas, S.; Kar, A.K. Photocatalytic Performance of Hydrothermal Temperature Dependent Dip Coated TiO_2 Thin Films. *J. Sol-Gel Sci. Technol.* **2022**, *102*, 649–664. [CrossRef]

42. Kim, S.H.; Lee, S.W.; Lee, G.M.; Lee, B.-T.; Yun, S.-T.; Kim, S.-O. Monitoring of TiO_2-Catalytic UV-LED Photo-Oxidation of Cyanide Contained in Mine Wastewater and Leachate. *Chemosphere* **2016**, *143*, 106–114. [CrossRef]

43. Lv, K.; Fang, S.; Si, L.; Xia, Y.; Ho, W.; Li, M. Fabrication of TiO_2 Nanorod Assembly Grafted RGO (RGO@TiO_2-NR) Hybridized Flake-like Photocatalyst. *Appl. Surf. Sci.* **2017**, *391*, 218–227. [CrossRef]

44. Liang, X.; Tao, H.; Zhang, Q.; Chang, C.-T. High Performance Photocatalytic Degradation by Graphene/Titanium Nanotubes Under Near Visible Light with Low Energy Irradiation. *J. Nanosci. Nanotechnol.* **2015**, *15*, 4887–4894. [CrossRef] [PubMed]

45. Chiang, K.; Amal, R.; Tran, T. Photocatalytic Oxidation of Cyanide: Kinetic and Mechanistic Studies. *J. Mol. Catal. Chem.* **2003**, *193*, 285–297. [CrossRef]

46. van Grieken, R.; Aguado, J.; López-Muñoz, M.-J.; Marugán, J. Photocatalytic Gold Recovery from Spent Cyanide Plating Bath Solutions. *Gold Bull.* **2005**, *38*, 180–187. [CrossRef]

47. Yang, L.; Jia, F.; Song, S. Recovery of $[Au(CN)_2]^-$ from Gold Cyanidation with Graphene Oxide as Adsorbent. *Sep. Purif. Technol.* **2017**, *186*, 63–69. [CrossRef]

48. Tsuchida, N.; Muir, D.M. Studies on Role of Oxygen in the Adsorption of $Au(CN)_2^-$ and $Ag(CN)_2^-$ onto Activated Carbon. *Metall. Trans. B* **1986**, *17*, 529–533. [CrossRef]